Delft University of Technology

Influence of process-based, stochastic and deterministic methods for representing heterogeneity in fluvial geothermal systems

Major, Márton ; Daniilidis, Alexandros; Hansen, Thomas Mejer; Khait, Mark; Voskov, Denis

Important note
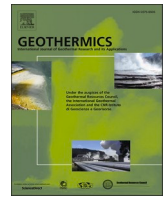To cite this publication, please use the final published version (if applicable).
Please check the document version above.

Influence of process-based, stochastic and deterministic methods for representing heterogeneity in fluvial geothermal systems

Márton Major [a], Alexandros Daniilidis [b,c,*], Thomas Mejer Hansen [a], Mark Khait [c,d], Denis Voskov [c,e]

[a] *Department of Geoscience, Aarhus University, Denmark*
[b] *Geo-Energy Reservoir Geology and Sedimentary Basin Analysis Group, University of Geneva, Switzerland*
[c] *Department of Civil Engineering and Geosciences, Technical University of Delft, the Netherlands*
[d] *Stone Ridge Technology S.R.L., Milan, Italy*
[e] *Energy Resources Engineering Department, Stanford University, USA*

ABSTRACT

Focus is on comparing stochastic, process-based and deterministic methods for modelling heterogeneity in hydraulic properties of fluvial geothermal reservoirs. Models are considered a generalized representation of a fluvial sequence in the upper part of the Gassum Formation in northern Denmark. Two ensemble realizations of process-based and stochastic heterogeneity were simulated using the state-of-the-art numerical modelling software, Delft Advanced Research Terra Simulator (DARTS), to assess differences on a statistically relevant sample size. Simulator settings were optimized to achieve two orders of magnitude improvement in simulation time. Our general findings show that the stochastic and process-based methods produce nearly identical results in terms of predicted breakthrough time and production temperature decline for high net-to-gross ratios (N/G). Simple homogenous and layered models overestimate breakthrough and underestimate temperature decline. More complex representation of facies in process-based models show smaller variance in results and stay within the limits of ensemble runs compared to simpler facies representation. Results indicate that a multivariate Gaussian based stochastic representation of heterogeneity provides comparable thermal response to a process-based model in fluvial systems of similar quality.

1. Introduction

Low-enthalpy geothermal systems are used for direct heating worldwide and their installed capacity has increased in recent years (Lund and Toth, 2020). Stefansson (2005) estimated more than 70% of geothermal resources are in water dominated environments with relatively low temperatures, below 150 °C. Therefore, deep sedimentary basins are ideal targets for geothermal exploitation, due to naturally occurring aquifers. Fluvial sediments especially are known to have good porosity and high permeability, ideal for thermal extraction. Sedimentary targets are commonly exploited using simple doublet configurations with production and reinjection (Gringarten, 1978; Mathiesen et al., 2020).

In geothermal systems, modelling accurate representations of the subsurface can improve the quality of simulated predictions. The need for considering variations in thermal parameters in regional modelling tasks has been highlighted by Fuchs et al. (2020); Fuchs & Balling (2016) and Poulsen et al., (2017) using inverse parameter calibration procedures (Hill and Tiedeman, 2007). In local models and shorter timescales, variations in hydraulic parameters control the evolution of a geothermal field (Vogt et al., 2010). Therefore, heterogeneity in hydraulic properties will have the largest impact on reservoir behaviour and is most often included in modelling studies (Hamm and Lopez, 2012; Wang et al., 2020; Willems et al., 2017). Techniques are available now to interpret seismic data, using rock physics modelling and make predictions to the porosity and permeability distribution in the reservoir (Bredesen et al., 2021; Feng et al., 2020). Deep sedimentary formations, suitable for geothermal extraction, however, often only have very limited number of boreholes and poor-quality seismic lines, making it difficult to use these advanced techniques. Therefore, most often some form of modelling is used to describe hydraulic properties.

Representing facies and hydraulic properties can be carried out

---

either with stochastic or process-based methods. Approximating reservoir facies using a stochastic approach has been extensively used in the hydrocarbon industry (e.g. Haldorsen and Damsleth, 1990; Keogh et al., 2007). The aim of stochastic modelling is to generate statistically realistic realizations from limited data by honouring the available data points and extrapolating to the rest of the formation using statistical rules. A collection of such realizations represents the model uncertainty, here the facies and hydraulic properties. Pixel based stochastic modelling can be based on multivariate Gaussian statistics that are described by choices of a mean and a covariance model (as we will consider here) or multiple-point statistics, that infer statistics from a training image. (Goovaerts, 1997; Remy et al., 2009). In other cases object-based modelling, which places objects such as sandstone bodies at random, has been the stochastic method of choice (Keogh et al., 2007; Larue and Hovadik, 2006). Using process-based models to simulate fluvial deposition, for a more realistic spatial distribution of facies, is another concept that arose early on (Bridge and Leeder, 1979). These models have the added advantage of relating net-to-gross (N/G) directly to the geometry of sandstone bodies. Early models, however, were often inapt due to limited knowledge of the governing sedimentary processes (Keogh et al., 2007). With more sophisticated codes available to accurately describe fluvial processes, such as the evolution of meandering channels, process-based methods are gaining more relevance recently (Cojan et al., 2005; Crosato, 2008; Flumy, 2019; Lopez et al., 2009).

Homogeneous and stratified reservoir models with multiple homogeneous layers have long been used for geothermal modelling purposes (Daniilidis et al., 2021, 2016; Poulsen et al., 2015; Saeid et al., 2014). In systems where subsurface data availability is sufficient, investigating the thermal response of more realistic reservoirs is gaining more attention (Babaei and Nick, 2019; Liu et al., 2019; Mottaghy et al., 2011; Wang et al., 2020; Zaal et al., 2021).

Crooijmans et al. (2016), showed that a model with random, uncorrelated facies distribution overestimates lifetime compared to process-based models for N/G below 70%. Above 70% N/G the different methods were in good agreement, but random models showed significantly lower variance in lifetime for a given N/G ratio. Babaei and Nick (2019) ran a large ensemble of models where they represented heterogeneity with a random Gaussian distribution and used different horizontal correlation lengths to assess the impact of lateral variability. They showed that including heterogeneity results in lower lifetime and high correlation length has the same effect. Moreover, recent studies have shown a significant overestimation of the thermal breakthrough time when upscaling highly heterogeneous fluvial reservoirs (Wang et al., 2023, 2020).

In this study we compare the dynamic thermal response of representing subsurface heterogeneity via a process-based, a stochastically generated and a deterministic, layered reservoir model based on log data. We present a systematic comparison of different methods to assess temperature and pressure evolution and utilize a target dataset to get the closest match between geological models created. We aim to compare the thermal response of realizations generated by stochastic simulation versus the process-based approach outlined above. All simulations are compared to deterministic representations, such as a homogeneous and a layered model. The two methods give comparable results across several metrics under high N/G conditions and reiterate that simplified models overestimate the lifetime of geothermal plants.

In the following, we introduce our dataset and the methods of process-based and stochastic simulation. Then we describe our model domain and the different scenarios used in this study and comment on computational efficiency. Thereafter, we present a short comparison of the different porosity fields and comment on the validity of our ensemble runs. Finally, the results of our study are discussed highlighting the key aspects of data analysis, which allow for conclusions to be drawn for similar environments.

2. Methods

The following section describes the methods used to carry out our simulations. First, we introduce background and dataset, followed by the process-based facies generation, then we explain the statistical method for populating the facies model with porosity values and generating our stochastic realizations; followed by a description of our homogeneous and layered cases to which we compare our process-based and stochastic simulations; and finally, we describe the process of geothermal simulation. Fig. 1 explains our full modelling workflow from the generation of geological models to geothermal simulation.

2.1. Background and input data

Process-based models were aimed to fit a general description of the upper part of the Gassum Formation in Denmark (Mathiesen et al., 2020; Weibel et al., 2017), where a sequence of the reservoir has been identified as mainly consisting of point bar deposits of meandering origin (Fig. 2, personal communication, Erik Skovbjerg Rasmussen, GEUS). Two boreholes are available from the Thisted area for estimation of N/G and porosity distribution (Fig. 2). Calculated effective porosity values of these boreholes were used to create the target file for statistical simulations. Data taken from two different boreholes are merged together to give a single distribution repsenting a general description of the sequence. We take this dataset as the basis of our models, but we extend

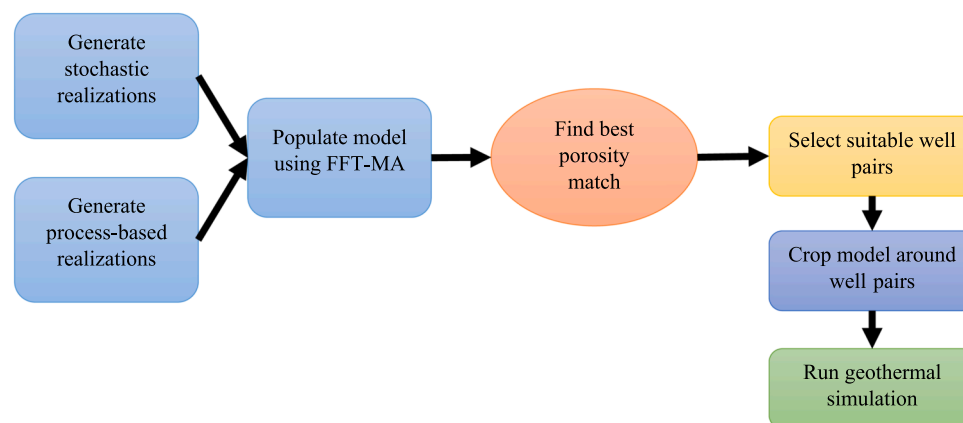
Fig. 1. Full modelling workflow for both the process-based and stochastic simulations. The geological models (both stochastic and process-based) cover a larger domain, from which a subset is cropped around the matching well pairs.
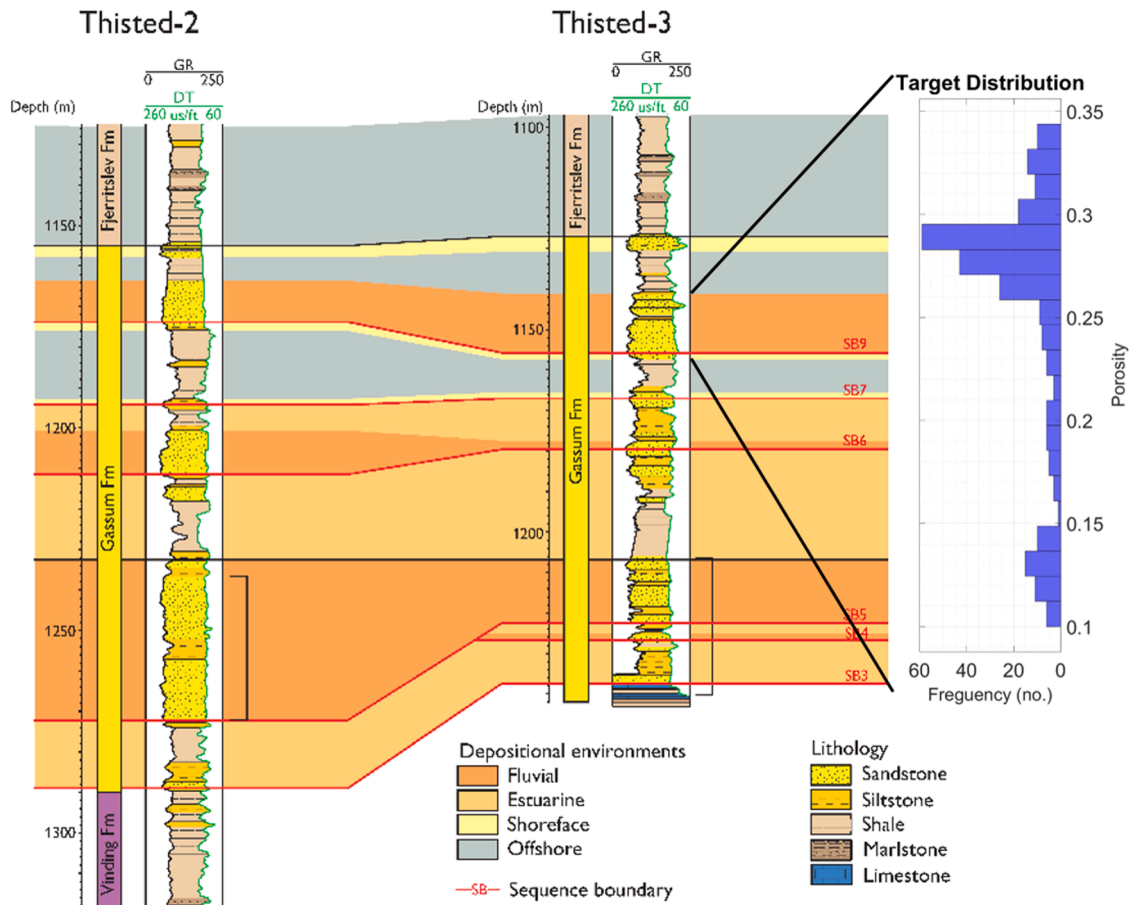
Fig. 2. Sequence correlation of the Thisted-2 and Thisted-3 boreholes and our target distribution. Target distribution is assembled from combined porosity data of the fluvial section above SB9 (modified from (Hjuler, 2014)).

the reservoir section to 50 m thickness (see section 3.1.1) and consider our realizations as imitating similar conditions. Models are not aimed to represent the exact situation in the Gassum Formation.

Porosity values were calculated using Gaussian methods as described in section 2.1.2. Porosity of the reservoir facies was then converted into permeability using a polynomial fit to data available from the Gassum Formation:

$$k = 196,449 \cdot (\Phi)^{4.3762},\tag{1}$$

where Φ is porosity (-) and k is permeability (mD). Permeability of clays was set to a constant value at 0.01 mD.

2.2. Static model spatial properties

2.2.1. Process-based facies model

For the process-based models, we used Flumy software (Flumy, 2019), which simulates deposition by meandering channels based on three processes: channel migration, aggradation processes, and channel wandering due to avulsions (Bubnova, 2018). The main hypothesis is that a meandering river can be described by a linear relationship between flow velocity close to the riverbank and lateral channel migration. Computer codes using this analogy have been remarkably successful in describing meandering channels for decades (Ikeda et al., 1981; Johannesson and Parker, 1989; Sun et al., 2001). In our study, the process-based workflow for creating facies realizations was similar to one used by (Crooijmans et al., 2016) and Willems et al., (2017) with the difference of using a Gaussian process to convert facies numbers to porosity distribution (see section 2.1.3). Main controlling parameters of the meandering channels were channel depth and width, maximum

overbank flood deposit thickness, avulsion frequency, flood frequency and a floodplain topography parameter (Willems et al., 2017). The latter designates the distance in meters at which the overbank deposit thickness decreases according to a negative exponential distribution (Flumy, 2019). Determination of the controlling parameters was based on a description of the paleo environment provided by the Geological Survey of Denmark and Greenland (GEUS) and boreholes available in the Thisted area (Fig. 2). Parameters were aimed to produce realizations with approximately 56% N/G and large, connected sandy facies (see Table 1). Flumy calculates N/G to be equal to the amount of point bar (PB) facies in the model. As we also categorized channel lags (CL), sand plugs (SP) and crevasse splays (CSI) as sands, the mean N/G value of our resulting realizations were 85% N/G with a standard deviation of 4%. Applying a 15% porosity cut-off to our target dataset, this is a reasonable value for this small section of the reservoir (Fig. 2).

Flumy outputs 9 different facies in fluvial mode in each model cell (Bubnova, 2018; Flumy, 2019) as seen on Fig. 3. To convert facies into

Table 1
Process-based simulation parameters.

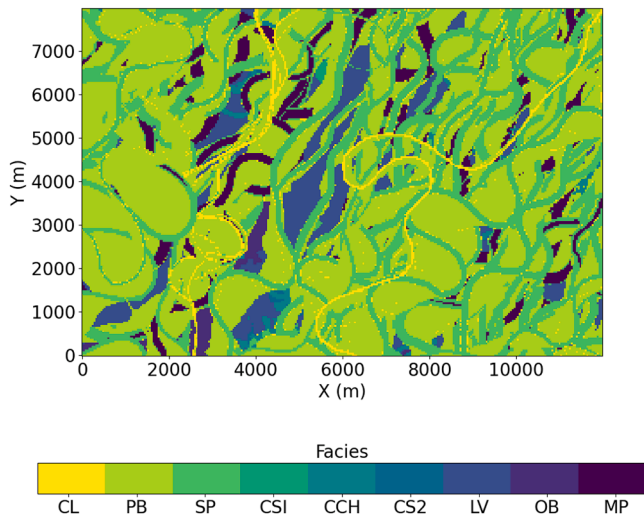|	
Channel width	300 m
Channel depth	10 m
Channel direction	30° from north
Overbank deposit thickness	0.3 m
Floodplain topography parameter	2800 m
Flood frequency	1000 years
Avulsion frequency	10,000 years

Fig. 3. Example of a single process-based realization showing the 9 different facies; Channel lag (CL), Point bar (PB), Sand plug (SP), Crevasse splay type 1 (CSI), Crevasse channels (CCH), Crevasse splay type 2 (CS2), Levee (LV), Overbank (OB) and Mud plug (MP).

porosity, we employed a Gaussian method and used the available borehole information as the target of statistical simulations as described in Section 2.2.2.

Porosity field of process-based models. To translate the facies numbers of the process-based models to a porosity field, we employed the fast Fourier transform moving average generator (FFT-MA), as implemented in the mGstat Matlab package (Hansen, 2022), which is an efficient numerical method to generate unconditional realizations of multivariate Gaussian distributions (le Ravalec et al., 2000). The normal score transform can be used to transform such realizations, with a 1D normal marginal distribution, to an arbitrary choice of 1D marginal distribution

(Goovaerts, 1997). The method allowed us to simulate porosity distribution based on a target sample, which we derived from boreholes in the Thisted area, Denmark (Fig. 2). Each simulation reproduced the distribution of this target dataset within the selected facies. The facies were categorised into reservoir (CL, PB, SP, CSI) and non-reservoir (CCH, CSII, LV, OB, MP) units in our ensemble runs and the reservoir group was divided into 4 additional categories (one for each sandy facies) in our more complex scenarios. Porosity within each facies was varied according to a covariance model to describe the spatial distribution in 3D. We used a spherical covariance model to better capture small scale variability and chose 400 m correlation length in the x-y direction for our sandy facies, as (Mottaghy et al., 2011) showed that largest variation is expected at ranges close to half the well distance. Since we represented all clays with a constant permeability in all our simulations, this property was not applicable to these facies. Correlation in the z direction was equal to the maximum channel depth assumed in our process-based realizations at 10 m (see Table 1). The simulation of the reservoir units was constrained to the target values from the boreholes, where a porosity cut-off above 15% was applied for the sand bodies.

2.2.2. Stochastic facies models

In our stochastic models, we used the truncated Gaussian method (Matheron et al., 1987) to create five distinct lithotype groups according to the mean ratio of the CL, PB, SP+CSI, MP facies and all other clays combined, taken from our process-based realizations. These five facies were then divided into 2 facies for our ensemble run (Fig. 4). We created an initial random Gaussian field (Fig. 4a) and lithotypes were obtained by splitting the total domain of variation into intervals, which then were assigned to the five distinct groups (Fig. 4b,) Beucher and Renard, 2016). The initial Gaussian simulation is generated using FFT-MA and the supposed direction of deposition (30° from north) was mimicked by an angular anisotropy factor of 3 along the flow direction. Lastly, the facies groups were separated into reservoir and non-reservoir units and FFT-MA was applied once more using our target file to determine the porosity distribution (Fig. 4c).
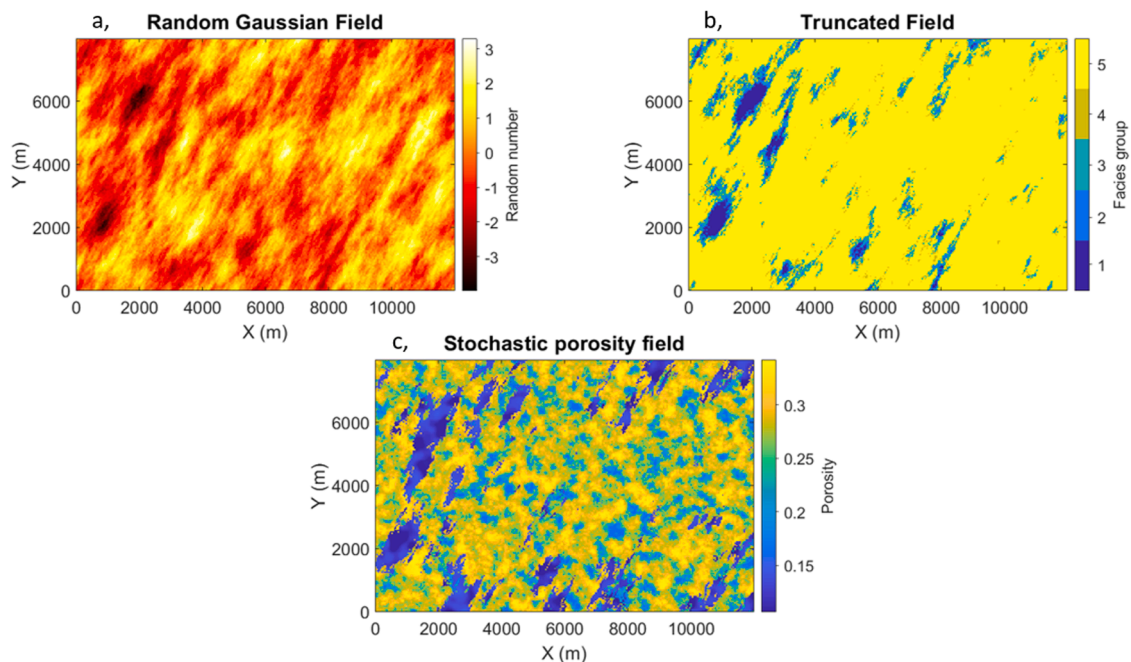

Fig. 4. Example representation of creating stochastic realizations using the truncated Gaussian method. a, randomly generated Gaussian field with angular anisotropy using FFT-MA; b, truncated field where values are divided into 'lithotype' groups; c, populated porosity field with reservoir and non-reservoir facies.

2.3. Geothermal simulation

For the purposes of geothermal modelling, we used the Delft Advanced Research Terra Simulator (DARTS, 2022), developed at the Technical University of Delft, the Netherlands. DARTS provides high accuracy and performance as shown in recent studies (Wang et al., 2020a, 2020b). These capabilities are available through the Operator-based Linearization (OBL) approach which effectively approximates complex governing physics without compromising on accuracy (Voskov, 2017). It employs discretization in the physical space in addition to the conventional temporal and spatial discretization. Operators are divided into two groups based on the physical state and spatial properties (Voskov, 2017). The former operators are represented in approximate form via physical supporting points and multilinear interpolation is used in between them, thereby simplifying the process, and turning the problem into a generic interpolation, calculated adaptively (Khait and Voskov, 2018). DARTS supports parallel execution on both CPU and GPU platforms to enable even faster simulation (Khait et al., 2020; Khait and Voskov, 2018). In the following, we describe the formulation of the governing equations, solved in the simulation process. The mass and energy balance for two-phase thermal simulation are as follows:

$$\frac{\partial}{\partial t}(\Phi \rho_w) - div\left(K\frac{\rho_w}{\mu_w}(\nabla p - \gamma_w \nabla D)\right) + \rho_w \widetilde{q}_w \sum_{j=1}^{n_p} \rho_j \widetilde{q}_j = 0, \tag{2}$$

$$\frac{\partial}{\partial t}(\Phi \rho_w U_w + (1-\phi)U_r) - div\left(Kh_w\frac{\rho_w}{\mu_w}(\nabla p - \gamma_w \nabla D)\right) + div(\kappa \nabla T)$$
$$+ \rho_w \widetilde{q}_w h_w$$
$$= 0, \tag{3}$$

where, ϕ is porosity, ρ_w is the water molar density, U_w is the water internal energy, U_r is the rock internal energy, h_w is the water enthalpy, k is the thermal conductivity, K is the permeability tensor, μ_w is the water viscosity, p is pressure, γ_w is the water gravity vector, D is depth, $\widetilde{q}_j$ is the phase rate per unit volume. Applying finite volume discretization and backward Euler approximation in time we get for Eqs. (2) and (3):

$$V\left((\Phi \rho_w)^{n+1} - (\Phi \rho_w)^n\right) - \Delta t \sum_l \left(\rho_w^l \Gamma_w^l \Delta \psi^l\right) + \Delta t \rho_w q_w \sum_j \rho_j q_j = 0, \tag{4}$$

$$V\left[(\Phi \rho_w U_w + (1-\phi)U_r)^{n+1} - (\Phi \rho_w U_w + (1-\phi)U_r)^n\right]$$
$$- \Delta t \sum_l \left(h_w^l \rho_w^l \Gamma_w^l \Delta \psi^l + \Gamma_c^l \Delta T^l\right) + \Delta t \rho_w q_w h_w$$
$$= 0, \tag{5}$$

where V is a control volume and $q_j = \widetilde{q}_j V$ is a source of phase j. Capillarity is neglected for simplicity and a Two-Point Flux Approximation is applied with an upstream weighting. Using these simplifications $\Delta \psi^l$ is the phase potential and ΔT^l is a temperature difference between blocks connected via interface l; $\Gamma_w^l = \Gamma^l k_{rw}^l/\mu_w^l$ is water transmissibility, where Γ^l is a constant geometrical part of transmissibility; $\Gamma_c^l = \Gamma^l \kappa$ is thermal transmissibility.

The terms in Eqs. (4) and (5) can be expressed as functions of physical state ω and/or spatial coordinate ξ. All state dependant operators are a function of physical state only, and therefore independent of spatial position, here the physical properties of the fluid and rock; space-dependant operators are a function of both physical state and spatial coordinate. Then the discretized mass conservation equation becomes:

$$\phi_0 V(\alpha(\omega) - \alpha(\omega_n)) + \sum_l \Delta t \Gamma^l \Phi^l \beta(\omega) + \theta(\xi, \omega, u) = 0, \tag{6}$$

where,

$$\alpha(\omega) = (1 + c_r(p - p_{ref})) \sum_{j=1}^{n_p} \rho_j s_j, \tag{7}$$

$$\Phi^l = (p^b - p^a) - \frac{\rho(\omega_1) - \rho(\omega_2)}{2} \gamma_w (D_b - D_a), \tag{8}$$

$$\beta(\omega) = \sum_{j=1}^{n_p} \rho_j \frac{k_{rj}^l}{\mu_j^l}, \tag{9}$$

$$\theta(\xi, \omega, u) = \Delta t \rho_w q_w \sum_j \rho_j q_j(\xi, \omega, u). \tag{10}$$

The discretized energy conservation reads:

$$\phi_0 V(\alpha_{ef}(\omega) - \alpha_{ef}(\omega_n)) + (1 - \phi_0)VU_r(\alpha_{er}(\omega) - \alpha_{er}(\omega_n))$$
$$+ \sum_l \Delta t \Gamma^l \Phi^l \beta_e(\omega) + \Delta t \Gamma^l (T^b - T^a) \sum_l (\phi_0(\varepsilon_{er}(\omega) - \varepsilon_{er}(\omega_n))$$
$$+ (1 - \phi_0)\kappa_r(\varepsilon_{er}(\omega) - \varepsilon_{er}(\omega_n))) + \theta_e(\xi, \omega, u) = 0, \tag{11}$$

where,

$$\alpha_{ef}(\omega) = (1 + c_r(p - p_{ref})) \sum_{j=1}^{n_p} \rho_j s_j U_j, \tag{12}$$

$$\alpha_{er}(\omega) = \frac{1}{1 + c_r(p - p_{ref})}, \tag{13}$$

$$\beta_e(\omega) = \sum_{j=1}^{n_p} h_j^l \rho_j \frac{k_{rj}^l}{\mu_j^l}, \tag{14}$$

$$\varepsilon_{ef}(\omega) = (1 + c_r(p - p_{ref})) \sum_{j=1}^{n_p} s_j \kappa_j, \tag{15}$$

$$\varepsilon_{er}(\omega) = \frac{1}{(1 + c_r(p - p_{ref}))}. \tag{16}$$

Here ω, ω_n are state variables of the current and previous time step, respectively; c_r is rock compressibility; p^a, p^b, T^a, T^b are pressures and temperatures, respectively, of grid block a and b connected through interface l.

This formulation allows for a simplified implementation of a complex framework. Complex physics are represented in an algebraic system of equations with abstract operators and the benefit is that all expensive calculations can be done at the pre-processing phase at a limited number of supporting points. Evaluation of the operators is then based on a multilinear interpolation, improving performance at the linearization stage (Khait and Voskov, 2018).

3. Model setup

3.1. Meshing grid

In order to get an accurate realization from Flumy, we selected a high vertical resolution of 0.2 m, as log data is available in 0.1 m increments, and a moderate resolution of 40 m horizontally. To be able to fully capture the meandering features we selected a domain of 12 km x 8 km x 50 m for the geological domain models. This resulted in 15 million cells for our geological model.

However, the full geological domain size will not affect the thermal response evaluation when a single doublet is active. Therefore, a smaller subdomain with dimensions of 4 × 4 km box around the midpoint between the wells was cropped to reduce the computational load (Fig. 5). The resulting thermal model, including over- and underburden extended 4 km x 4 km x 459 m and was comprised of 2.75 million control volumes. Midpoint reservoir depth is set to 1200 m.

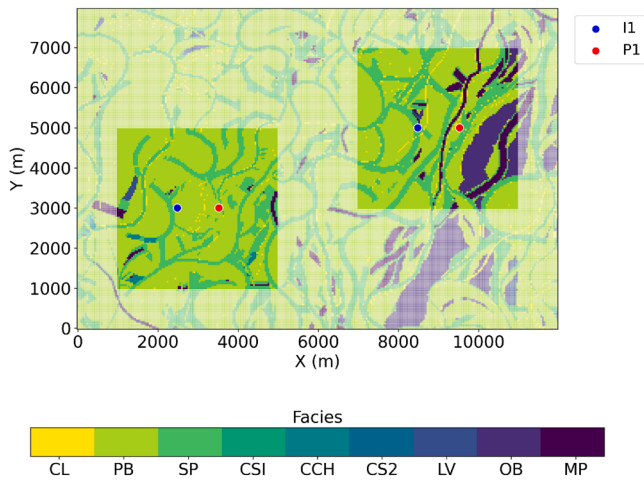Well placement was decided based on calculating the L2-norm of the

Fig. 5. Geological model from a process-based realization. Cropping of the thermal models is illustrated by the highlighted boxes around the well locations. Colour bar shows the different facies.

difference between the target dataset and the resulting porosity distribution in our model after population. We chose the best fitting 2% of model columns as possible borehole locations and then searched this area within a 10 m radius of the desired well spacing, 1040 m, to create well pairs. To avoid having well pairs positioned close to the geological model boundaries, a padding area of 1000 m from the edge of the geological model was excluded from the well pair selection domain.

3.2. Initial and boundary conditions

Initial conditions were set as a simple gradient between the top and bottom of the model for both temperature, at 30 K/km and pressure at 100 bar/km. This resulted in an average reservoir temperature of 319.2 K and pressure of 120 bar. Thermal conductivity and heat capacity of the matrix was set to 259.2 kJ/m/d/K and 2200 kJ/kg in the reservoir and set to 129.6 kJ/m/d/K and 2240 kJ/kg in the confining beds and non-reservoir units.

Rate-control was applied to both wells using a 4800 m^3/d flow rate boundary condition and injection temperature was set to 284.15 K. In the range of pressure and temperature used in our models the resulting density differences between injection and production are below <1.6%. Boundary conditions on the sides of the model were set to a constant pressure and temperature equal to initial conditions defined by the respective gradients. Each model simulation was run for 100 years. Table 2 summarizes thermal parameters of our model setup.

Table 2
Parameters of the thermal model.

Parameter	Value
dx/dy/dz (m)	40/40/0.2
Cells ($\times 10^6$)	2.75
Porosity distribution	Process-based/Stochastic
Permeability clay/sand (mD)	0.01/Eq.(1)
Thermal conductivity clay/sand (kJ/m/d/K)	129.6/259.2
Heat capacity clay/sand (kJ/kg)	2200/2240
Well spacing (m)	1040
Rate (m^3/d)	4800
Injection temperature (K)	284.15

Table 3
Overview of scenarios and their main parameters.

Scenario	No. of facies groups	Porosity distribution	Flow rate (m^3/d)	No. of simulations
Pb2f	2 (sand, clay)	Variable	4800	1863
St2f	2 (sand, clay)	Variable	4800	1829
Pb5f	5 (4 sands, 1 clay)	Variable	4800	11
Pb5c	5 (4 sands, 1 clay)	Constant within each facies	4800	11
Pb2f_x	2 (sand, clay)	Variable	2400, 3600, 6000	33
St2f_x	2 (sand, clay)	Variable	2400, 3600, 6000	33
Base case	1	Homogeneous	4800	1
Layered case	1	Constant in each layer	4800	1
Total number of simulations				3782

3.3. Scenario descriptions

All our scenarios were compared to two simplified cases. The first one assumed a homogeneous reservoir (Base case) and the second one employed a layered model (Layered case). In the latter, the porosity of each reservoir layer corresponded to a value taken from an averaged target file to fit the number of layers in our reservoir model. Table 3 summarizes the main parameters of our different scenarios.

3.3.1. Scenario process-based, 2 facies (Pb2f)

Our first scenario describes the process-based cases using 2 facies. We generated 100 geological models using Flumy, separated facies into sand and clay groups and populated the domain with porosity values (see section 2.1.2.2). From the populated geological models, we selected the 10 best fitting ones based on an L2-norm fit to our target distribution. In the selected geological models, the best 2% of columns in each realization were selected, and well pairs were picked within a 10 m radius of our desired well spacing of 1040 m. The geological model was then cropped around the wells as described in section 3.1.1 (cf. Fig. 3). These operations resulted in 1863 suitable thermal models.

3.3.2. Scenario stochastic, 2 facies (St2f)

This scenario contains the stochastic models where 200 geological models are generated using the truncated Gaussian method. Reasons for needing double the amount of realizations compared to Pb2f are discussed in Section 4.1. We again only differentiated between two separate facies (sand and clay) and picked out the 20 best fitting geological realizations to our target. Similar to Pb2f we selected the top 2% of model columns and found suitable well pairs within 1035 – 1045 m distance from each other. Hereafter, we cropped the geological model to the described extent. This process resulted in 1829 thermal models for this scenario.

3.3.3. Scenario process-based, 5 facies (Pb5f)

To investigate the effect of small-scale heterogeneity, we selected 11 thermal models, which closest approximated 9 evenly spaced percentiles (P10-P90) and the best and worst cases of our Pb2f scenario and ran simulations with the added complexity of 5 different facies. This allowed us to capture the overall variability of the ensemble runs. We differentiated between four types of sandy facies (CL, PB, SP, CSI) and one additional group combining all clays. As we assumed our model to be mainly consisting of point bars, they were modelled to fit our target distribution (Fig. 2). Other sand facies, CL, SP, CSI were represented with a random uniform distribution with mean porosities of 0.26, 0.22

and 0.15, respectively. These values were selected to preserve the mean value of our original target distribution.

3.3.4. Scenario process-based, 5 facies, constant porosity (Pb5c)

Similar to Pb5f, the 11 selected thermal models were run with 5 facies. In this case, we represented each facies with a constant porosity value and picked values to preserve the weighted mean porosity of our target distribution (Fig. 2). The exact values were CL = 0.26, PB=0. 32, SP=0.22, CSI=0.15 and clays = 0.1.

3.3.5. Scenario process-based, 2 facies, rates (Pb2f_x)

As in Pb5f, we selected 11 models representing the best and worst case scenario and 9 evenly spaced percentiles of Pb2f and ran the thermal models with discharge rates of 2400 m^3/d, 3600 m^3/d and 6000 m^3/d, respectively. Simulations in this scenario were compared to those of Pb2f.

3.3.6. Scenario stochastic, 2 facies, rates (St2f_x)

To assess the influence of discharge rate on our simulations we took the same 11 models from St2f and ran them with rates of 2400 m^3/d, 3600 m^3/d and 6000 m^3/d, respectively. These simulations were examined in relation to variability in breakthrough time and spread in temperature decline.

3.4. Computational efficiency

Special attention was paid to minimize the time required to run our ensemble models. DARTS platform was deployed, since it provides unique capabilities for simulating geothermal models entirely on GPU (Wang et al., 2020a, b). In addition, both model initialization and simulation were optimized (see **Appendix**).

The improvements described in **Appendix** reduced the initialization time of each model down to only 3.74 s on average, where nearly half of the time was spent on transmissibility calculations. The simulation time of a single model varied from 85 to 128 s, taking 102 s on average. The total time for processing of a single model, including initialization, simulation, finalization and corresponding overheads was 116 s on average.

All the models were added to a pool of jobs, which were dispatched on one of 6 available GPUs, a single model per GPU, therefore 6 models were processed simultaneously. Taking this into account, the average time of running a single model was only 19.47 s, allowing to process all 3692 ensemble models in just under 20 h. This was an improvement of 2 orders of magnitude compared to simulation time on a single CPU.

4. Results and discussion

4.1. Porosity fields comparison

Fig. 6 shows a comparison of the resulting porosity fields from four different scenarios. The most obvious difference between St2f and Pb2f (Fig. 6a and b) is in the distribution, shape and size of the clay facies as the stochastic realization cannot capture the sinusoidal mud plug structures or the overbank 'islands' accurately. Instead, bigger patches aligned according to our chosen anisotropy direction of 30° from north are observed. In terms of the sandy facies, there is no clear difference between these two at first glance as both were populated using the same target distribution and correlation length.

Dividing the sandy facies into 4 different groups does change the porosity distribution quite a bit, as high porosity point bars are now less connected and channel features are more evident due to the separation of sand plug facies (Fig. 6c). Using constant values for the 5 facies in Fig. 6d clearly highlights the large amount of point bars and eliminates the lower porosity features present in Fig. 6c within the point bar facies, which stem from the matching of our target distribution. Important to note is the absence of CSI from Fig. 6d. This is due to a systematic
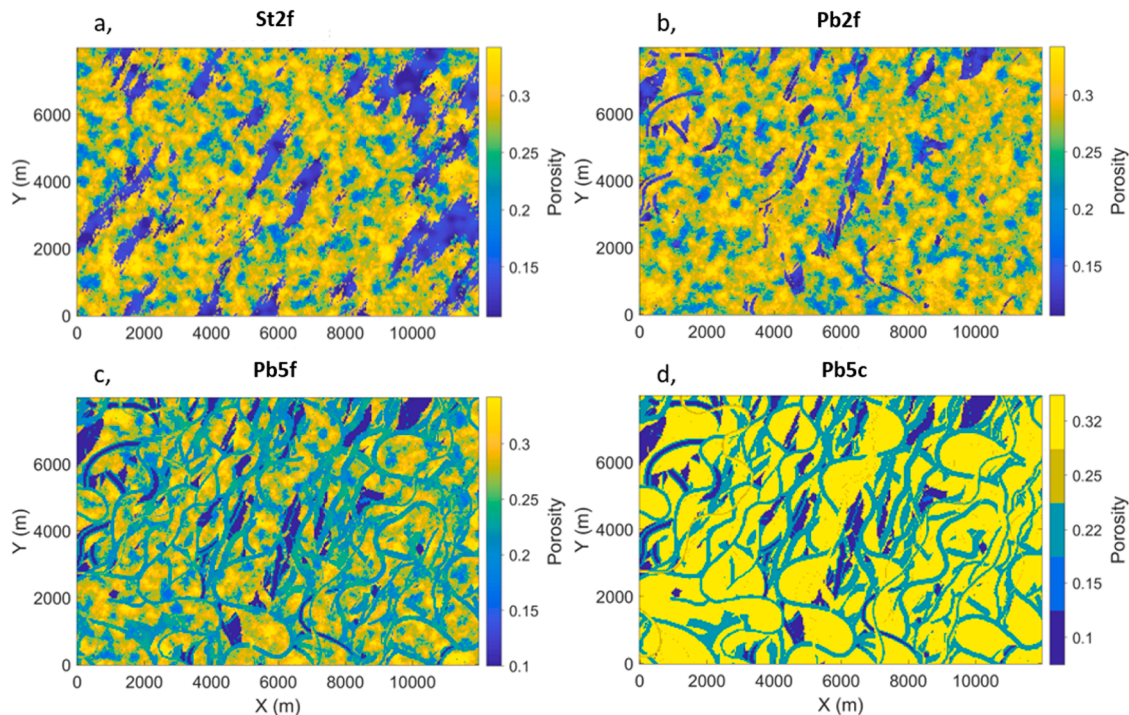

Fig. 6. Porosity distribution of selected realizations from a, St2f; b, Pb2f; c, Pb5f and d, Pb5c. The constant porosity values of the colour scale in d, correspond to the different facies, from top to bottom PB, CL, SP, CSI and clays.
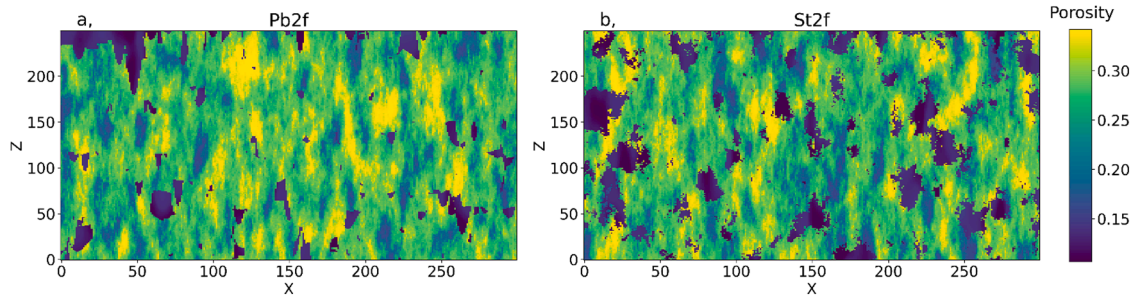
Fig. 7. Example plot of porosity cross-sections along the x-axis of the reservoir domain from a, Pb2f and b, St2f. Axes show number of cells and z-axis is exaggerated 5 times for readability.
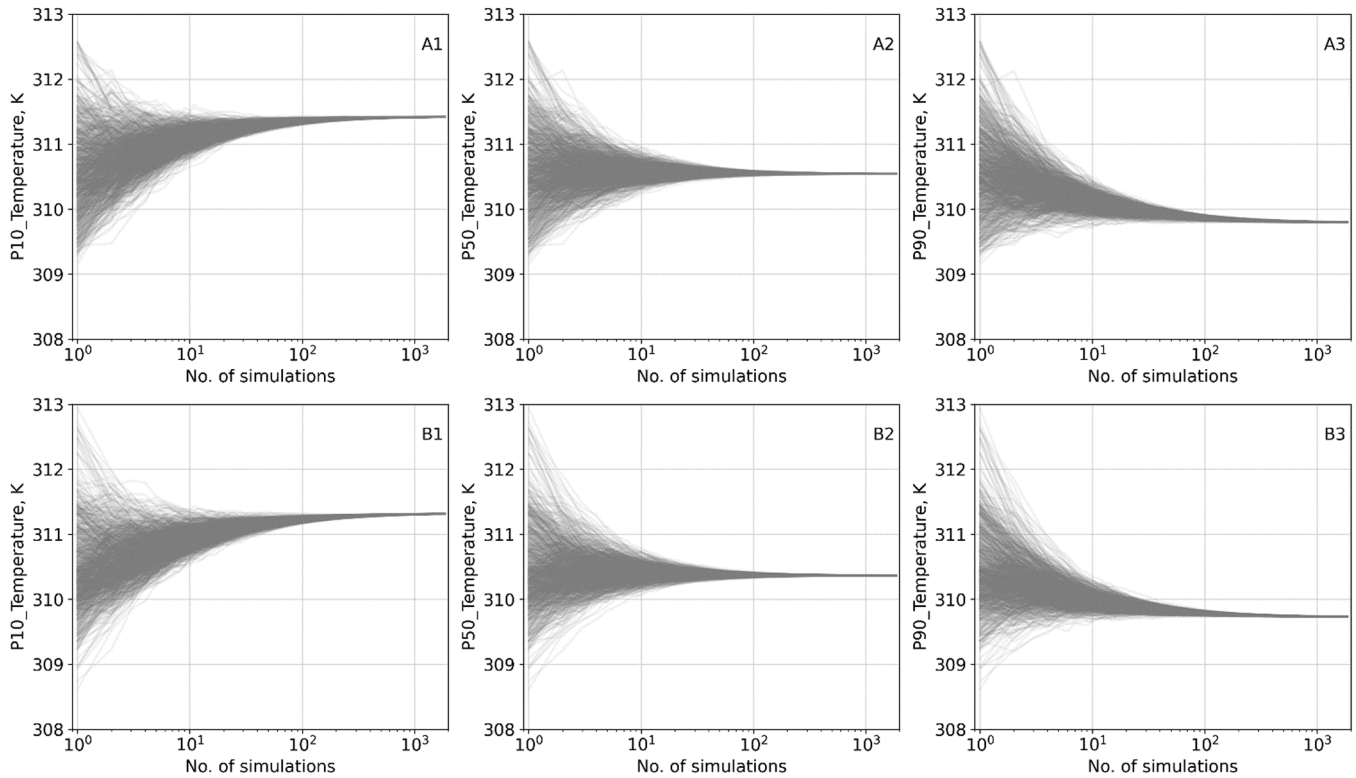

Fig. 8. Moving average of P10, P50 and P90 of production temperature after 100 years for scenarios Pb2f and St2f with increasing number of realizations. A1, A2 and A3 are showing P10, P50 and P90 of Pb2f, respectively; B1, B2 and B3 are P10, P50 and P90 of St2f, respectively.

underrepresentation of this facies in our process-based realizations, which we could not resolve despite our best efforts.

Vertical cross-sections of porosity values along the x-axis from an example of Pb2f and St2f are shown in Fig. 7. The clay facies with low porosity have very different shapes and extent on the two plots. On the one hand, Pb2f mainly produces thin, U-shaped clay deposits corresponding to mud plugs in abandoned channels and some thin layers of overbank facies, mostly on the top of the reservoir (Fig. 7a). In contrast, St2f has clay patches with different shapes and sizes, but generally wider and more evenly distributed in the domain. The differences in clay facies shape and distribution between Figs. 6 and 7 explains why St2f produces approximately half the amount of suitable thermal models per realization compared to Pb2f. The wider, more evenly distributed clay patches disrupt the continuity of sandy facies and can make it more difficult to find good matches to our target at a given distance (see section 3.1.1).

4.2. Result convergence

To validate that convergence is achieved for our ensembles the moving average of P10, P50 and P90 of production temperature after 100 years for both Pb2f (Fig. 8A1, A2, A3) and St2f (Fig. 8B1, B2, B3) versus the number of simulations (Fig. 8) was calculated. After an ensemble of 500 simulations, the expected value of P10, P50 and P90 does not change significantly for either scenario and they correspond well with the values seen on Fig. 9 at 100 years. Therefore, sufficient thermal simulations are performed to be able to draw statistically relevant conclusions.
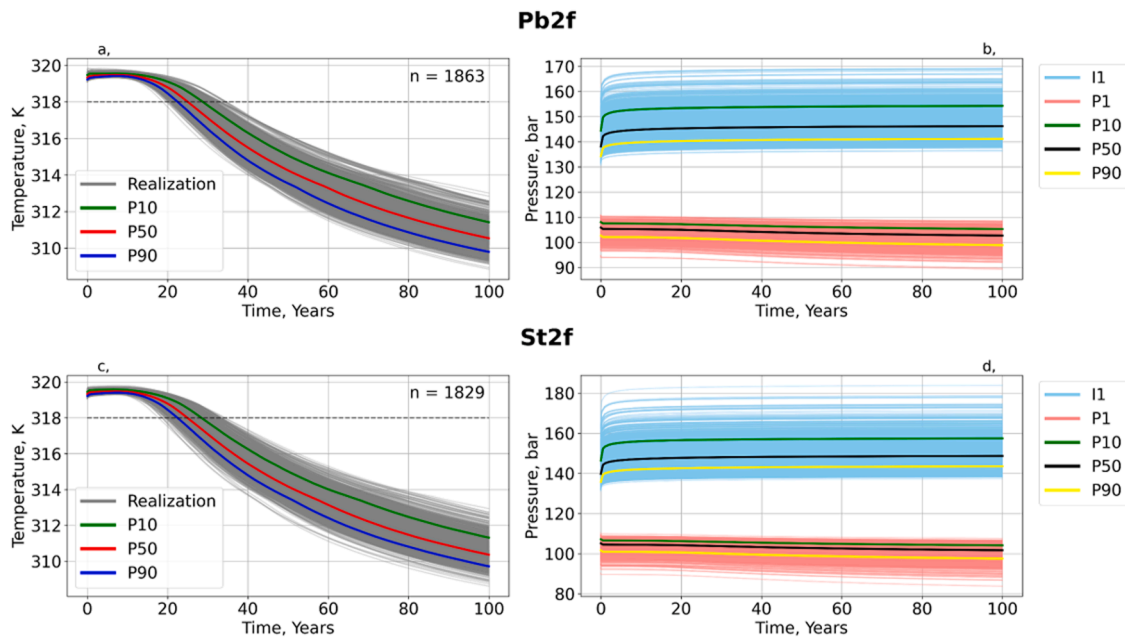
Pb2f

St2f

Fig. 9. Production temperature and pressure for all process-based (a, b) and stochastic realizations (c, d) in Pb2f and St2f, respectively. The dashed grey line represents the point of thermal breakthrough, considered as a temperature drop of 1 K from the initial production temperature.

4.3. Well pressure and temperature

Fig. 9a and c show production temperature for all simulations after 100 years, from both Pb2f and St2f. We designate breakthrough to occur at the time production temperature has decreased 1 K from the starting temperature, in this case, when reaching 318 K for readability. In Pb2f, the spread in breakthrough time is approximately 16 years, and varies between 18.6 years and 34.6 years, while scenario St2f gives almost identical extremes at 18.6 and 34.2 years, respectively. This result is different from the findings of Crooijmans et al., (2016) who found a random, uncorrelated model to give significantly smaller spread in lifetime than a process-based counterpart. However, Crooijmans et al., (2016) did not investigate convergence of their ensemble dataset. Moreover, our stochastic model uses our target file for matching porosity distribution and a spherical covariance function with 400 m correlation length in x-y and 10 m in z direction (see section 2.1.2.2). Therefore, we

expect to get a better match to our process-based models. Fig. 9b and d show pressure evolution in both I1 and P1 for the two scenarios. Here we see that the stochastic simulations (Fig. 9d) exhibit about 12 bars higher maximum pressures in I1 as the process-based counterpart (Fig. 9b). This pressure difference is not as apparent in median values however, which only show 1–2 bar higher expected pressure for stochastic simulations. Observing higher maximum pressures can be attributed to bigger clay patches in the stochastic models which can affect the flow path and decreasing reservoir hydraulic conductivity (Figs. 6a and 7b) a similar effect is described by Crooijmans et al. (2016).

Fig. 10 compares the P10, P50 and P90 of the ensemble runs to the Base and Layered cases. The layered and homogeneous temperature curves are almost identical, and they match well with the P10 curve of Pb2f and St2f for both breakthrough time (~28 years) and temperature decline after 100 years. This suggests that the simplified models overestimate the breakthrough time of the reservoir, on average, by about 3 years and the temperature decline by ~1 K. Comparing Pb2f and St2f scenarios directly, all percentiles, are very close to each other in terms of breakthrough time, which occurs after 22.6, 25.1, and 28.6 years for Pb2f and 22.6, 25.1, and 28.1 years for St2f, respectively. These similar values imply that when using only two distinct facies with a high N/G, a well-designed stochastic method will give the same expected result as using a process-based approach. Given that generating stochastic realizations is considerably faster than running process-based models, we can argue that in cases where conditioning data points are available and at high N/G ratios, using stochastic models is preferable. Even after taking into account the extended computation time associated with the fact that we needed twice as many realizations to get similar number of models matching our criteria. After breakthrough, the curves show a similar trend overall and the production temperatures after 100 years stay slightly higher for all three percentiles of Pb2f shown, with predicted temperatures staying within ~0.3 K (Fig. 10).

Example realizations from both scenarios Pb2f and St2f are shown with production temperatures on Fig. 11a, c and the permeability distribution with corresponding well locations on Fig. 11c, d. This figure illustrates well the discrepancy between the number of suitable well pairs per realization as discussed in Section 4.1. Due to this discrepancy, we see higher variance in the production temperatures of the process-
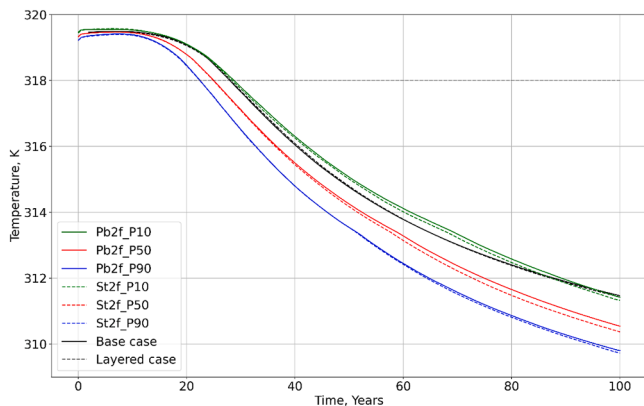

Fig. 10. Comparison of production temperature evolution for the Base (solid black curve) and Layered (dashed black curve) cases to selected percentiles of our ensemble runs. a, showing P10, P50 and P90 of Pb2f with solid lines; b, showing P10, P50 and P90 of St2f with dashed lines.
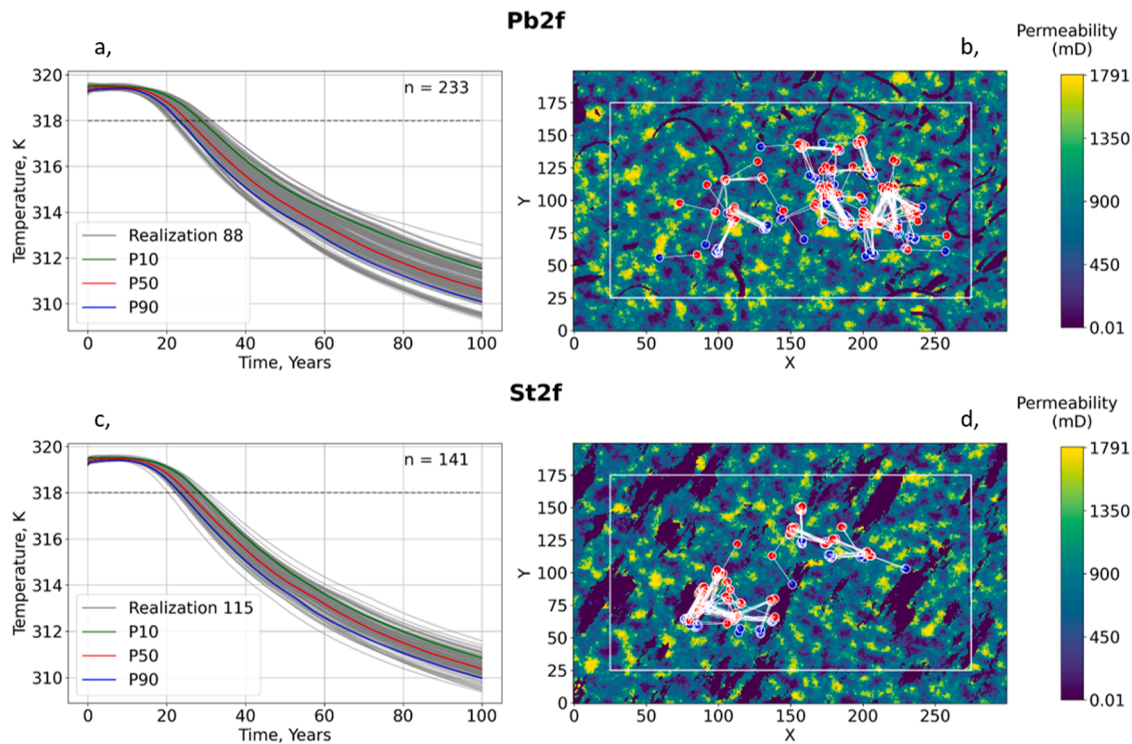
Fig. 11. Examples of one realization from Pb2f and St2f respectively. a, showing production temperature with time and b, showing the corresponding permeability field with borehole locations for Pb2f; c, showing production temperature and d, showing permeability and borehole locations for St2f. White rectangle denotes the padding distance chosen to avoid placing wells near the sides of our domain.

based models, which highlights the importance of running several different realizations. It is again noticeable on the permeability plots how the structure of the clay facies is different between the two methods. We see two clusters of suitable well pairs in St2f (Fig. 11d) versus a more even distribution for Pb2f (Fig. 11b).

4.4. Reservoir pressure and temperature

Reservoir pressure and temperature evolution, along with porosity distribution are shown in Fig. 12 for the most extreme cases of scenarios Pb2f and St2f. The figure shows a slice from the middle of our reservoir domain at 1200 m depth. We define worst case as showing largest decline in production temperature after 100 years and best case as showing the highest production temperatures at the end of the simulation. Fig. 12A shows the worst case of Pb2f. From Fig. 12A1 it is clear that no low porosity areas obstruct the flow between the two boreholes, which allows easy connection between P1 and I1 and leads to quick breakthrough and large temperature decline. We get a pear-shaped cold plume which extends more into the high porosity areas, mainly to the east of I1 (Fig. 12A3, A4). On Fig. 12B1 we can see generally lower porosity values between the boreholes and some distinct clay patches which slow down the cold plume and a considerable part of the flow diverted from the producer to the west of I1 (Fig. 12B3, B4). The expansion of the plume is especially hindered to the south of the doublet, where the low porosity has a larger, connected area. Therefore, we get a slower decline in temperatures. For the worst case in St2f (Fig. 12C), I1 is located in a low porosity patch which extends far out to the southwest of the well (Fig. 12C1). Yet, the plume shape seems symmetric and fairly

regular, though considerably slimmer in the east-west direction (Fig. 12C3 and C4). The slim plume shape indicates that the water finds a narrow band of high permeability sands connecting the boreholes and flow is concentrated in these leading to high Darcy velocity and larger temperature decline. The best case of St2f is shown on Fig. 12D. I1 is situated right at the border of a bigger low porosity area and a smaller clay patch, right at P1 (Fig. 12D1), seems to restrict flow considerably (Fig. 12D3, D4). This is especially visible on the 50-year plot, where the plume to the north of our doublet is significantly smaller than to the south (Fig. 12D3). This effect is less pronounced after 100 years (Fig. 12D4). Fig. 12D2 shows that pressures are also elevated compared to the worst case of St2f (Fig. 12C2), which we expect for a lower permeability field.

4.5. Cold front position

Taking a 1 K temperature drop compared to initial reservoir temperature as the indicative position of the cold front, a good match between the process-based and the stochastic simulations is observed (Fig. 13). For both types of heterogeneity representation, a higher concentration of contours is apparent close to the production well (Fig. 13A1, B1). Most deviations are observed in the western part of the domain, along the well plane and to the west of the injector, where the range of the cold front position is about 500 m for Pb2f and up to 650 m for St2f. In all other directions the cold front position is contained within a circa 250–300 m band for both types of heterogeneity representation.

Individual simulations of St2f that move away from the bulk of the contours have a more pronounced and directional shape compared to
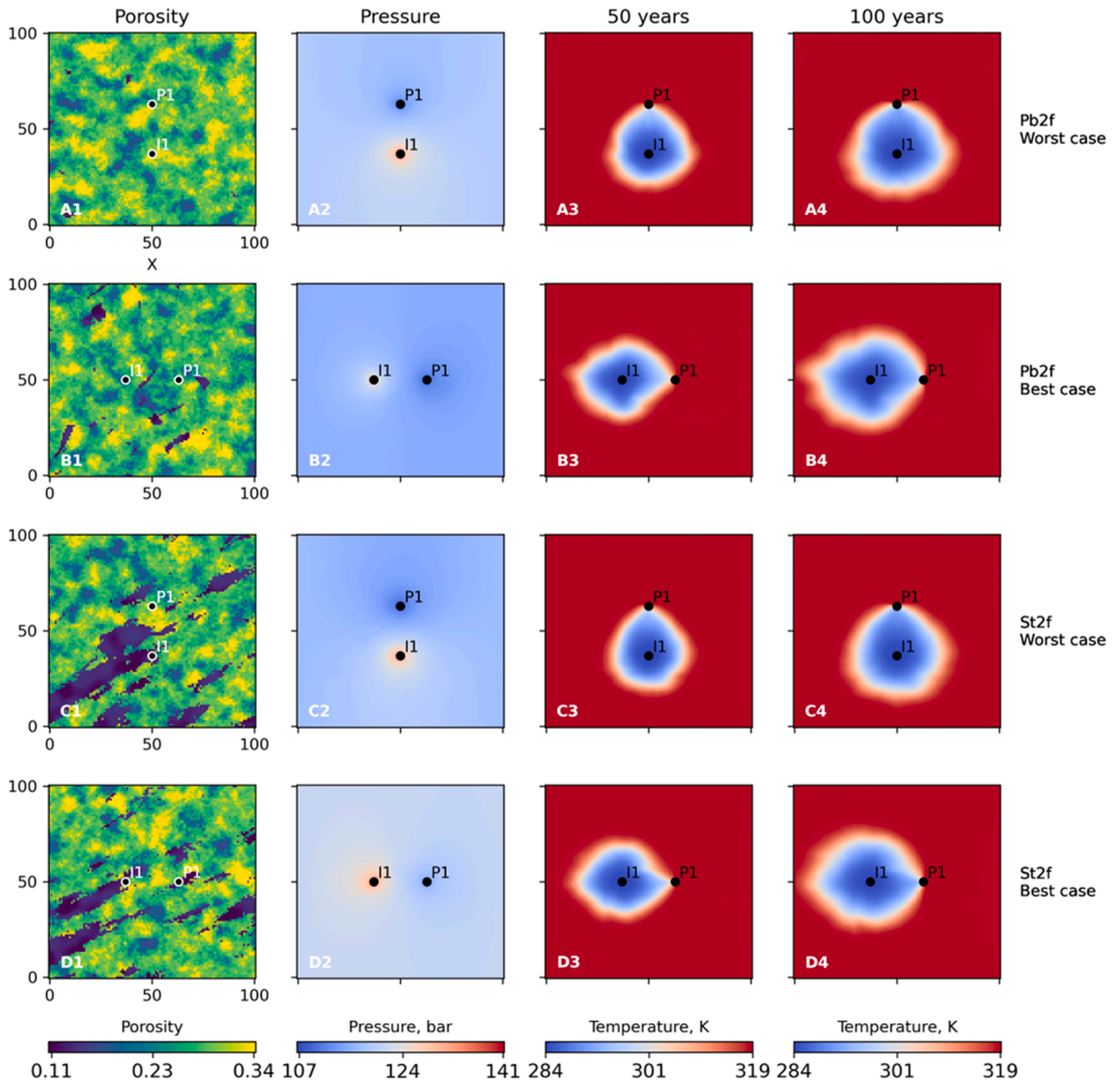
Fig. 12. Horizontal cross-sections across the middle of the reservoir for best and worst cases of Pb2f (A, B) and ST2f (C, D) scenarios showing porosity field (A1, B1, C1, D1), pressure distribution (A2, B2, C2, D2) and extent of the cold plume after 50 (A3, B3, C3, D3) and 100 years (A4, B4, C4, D4).

the individual realizations of Pb2f that appear more rounded with a less pronounced directional pattern (Fig. 13A1, B1). The vertical sections across the well plane show again a strong concentration of contours on the position of the producer (Fig. 13A2, B2). The largest differentiation is observed to the west of the injector well. Similar to the horizontal cross-section, the vertical cross-section also shows a larger variability for the stochastic simulations (Fig. 13A2, B2).

4.6. Small-scale variability impact

Fig. 14 shows the comparison of our simulations including 5 facies (Pb5f and Pb5c) to our process-based ensemble run (Pb2f). The 11 models were chosen to be closest to 9 (P10-P90) evenly spaced percentiles of Pb2f, along with the two extreme cases, to represent the full variability of the ensemble.

For both Pb5f and Pb5c scenarios, their respective ensemble spread is fully contained within the Pb2f percentile range throughout the whole 100-year period. Scenario Pb5f shows lowest variability both in terms of breakthrough time and overall temperature decline. Our original ensemble, Pb2f, shows a larger spread in both subplots, whereas Pb5c lies in between the other two. Including 5 facies seems to improve lifetime overall, as both Pb5f and Pb5c retain higher production temperatures after 100 years than Pb2f. In the case of Pb5f, breakthrough time is also slightly delayed, while retaining higher temperatures at the end of 100 years. We attribute this behaviour to the impact of small scale variability within facies, which introduces small areas of lower than average permeability where Darcy velocity decreases and thermal recharge can be higher resulting in delayed breakthrough (Daniilidis et al., 2020b; Wang et al., 2021).
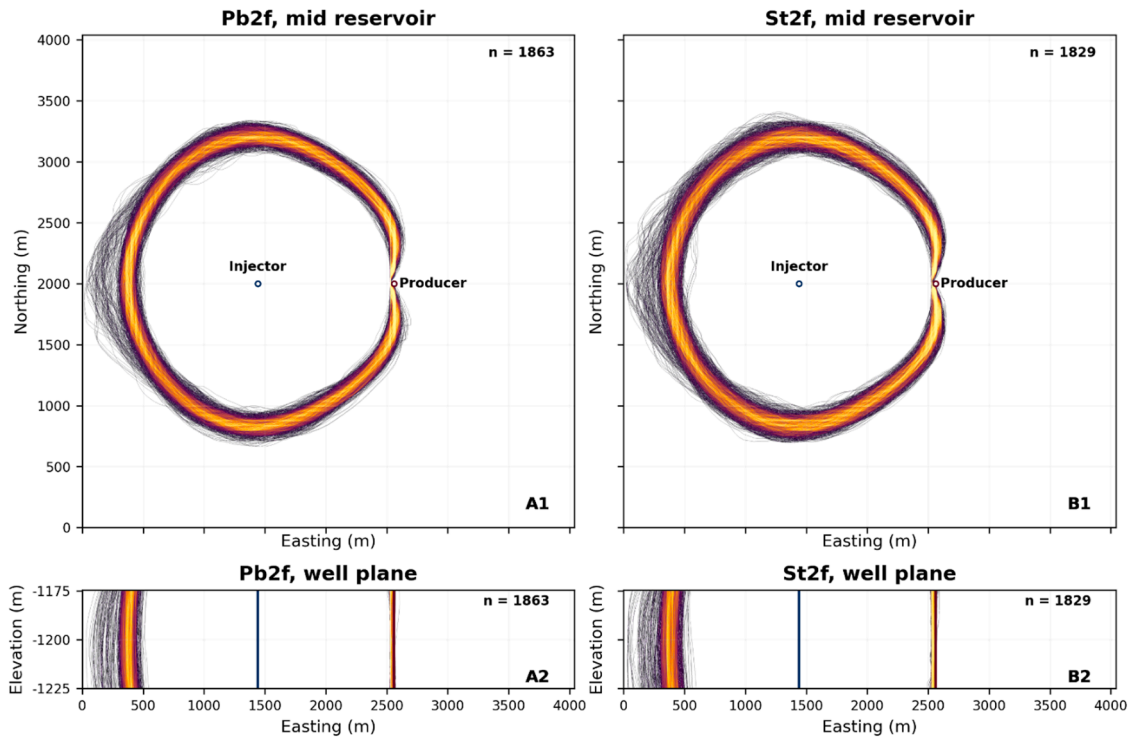
Fig. 13. Heat map of the contours showing a 1 K temperature drop compared to initial reservoir temperature for all simulations of scenarios Pb2f and St2f for a horizontal cross section across the middle of the reservoir (A1, B1) and a vertical cross section across the injector and producer well plane respectively (A2, B2). A lighter colour indicates higher density. All simulation data regardless of initial well orientation is aligned with the position of the injector and producer well along the Easting axis. Data is shown after 100 years of production for all plots. Injector and producer wells presented in red and blue colours respectively.
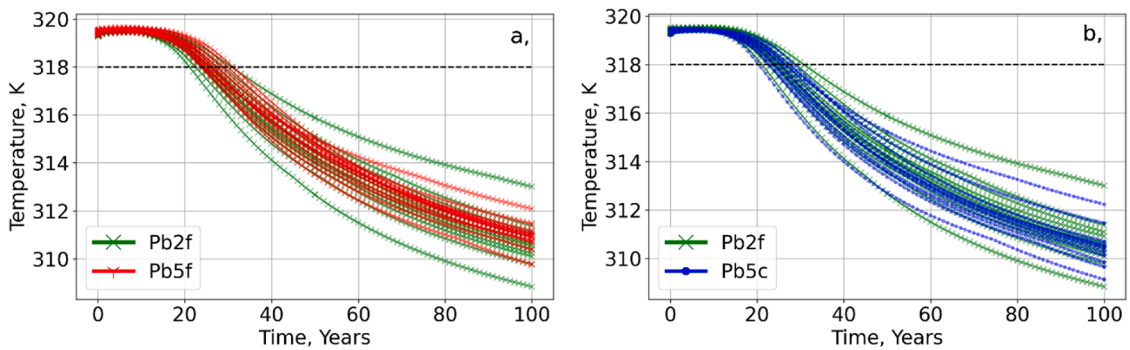

Fig. 14. Comparison plot of production temperatures for the process-based scenarios. a, comparing Pb2f (green curves) to Pb5f (red curves); b, comparing Pb2f (green curves) to Pb5c (blue curves). Black dashed lines highlight the temperature at which we designate breakthrough to occur.

4.7. Flow rate impact

To gain an insight into the effect of flow rate on our results, selected models from Pb2f and St2f were run with flow rates of 2400 m³/d, 3600 m³/d and 6000 m³/d. Fig. 15 shows the production temperature with time for these simulations and Pb2f and St2f are compared for each flow rate value presented. For Pb2f, breakthrough is delayed due to the lower flow rates and the spread in breakthrough time is increased from about 16 years for 3600 m³/d, to 26 years for 2400 m³/d, whereas 6000 m³/d shows only a 5-year spread. Similarly, St2f shows highest spread in breakthrough for 2400 m³/d at 24.5 years and this is decreasing to 14.5 and 6 years, for the cases of 3600 m³/d and 6000 m³/d, respectively. These results are in line with the findings of other researchers (e.g.

Daniilidis et al., 2020a, 2016; Saeid et al., 2015), who showed that higher discharge rates produce sharper breakthrough curves and that discharge has the biggest influence on lifetime. Spread in production temperatures after 100 years is around 4 K at higher rates and drops to about 3 K when 2400 m³/d is used in both cases presented. We see a clear trend in these two scenarios, where the difference in spread of both breakthrough time and temperature decline is increasing with lower discharge rate. We explain this by the lower rates exaggerating the differences in flow inside the reservoir. St2f is consistently predicting bigger decline in temperatures for it's worst case compared to Pb2f and the two best case scenarios also separate at lower rates highlighting the subtle difference in reservoir construction (Fig. 15).
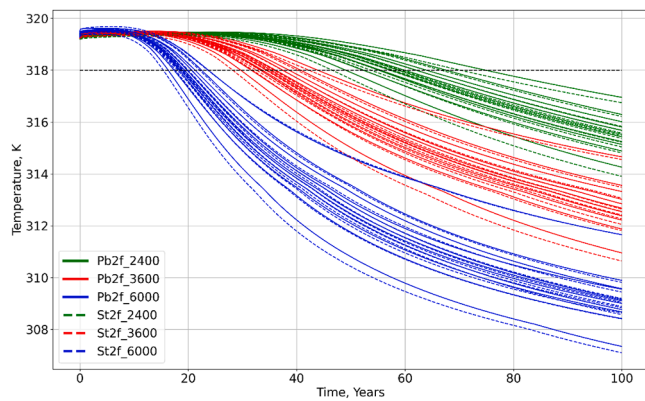
Fig. 15. Influence of production rate on the spread of production temperature decline and breakthrough time for scenarios Pb2f and St2f. Solid lines show Pb2f with rates of 2400 m^3/d (green curves), 3600 m^3/d (red curves) and 6000 m^3/d (blue curves), respectively. Dashed lines show St2f with rates of 2400 m^3/d (green curves), 3600 m^3/d (red curves) and 6000 m^3/d (blue curves), respectively. Black dashed line highlights the temperature at which we designate breakthrough to occur.

5. Summary and conclusions

We have compared a process-based and purely stochastic approach to deterministic models for representing heterogeneity in hydraulic properties of fluvial reservoirs, when a target distribution is drawn from log data. Our two ensemble runs were divided into reservoir and non-reservoir facies and two additional scenarios are investigated where the different sandy facies are separated in the geological model.

Our study highlights that DARTS is remarkably efficient in running large ensembles and initial running time for single simulation of a geothermal model with 5.5 million unknowns was improved by two orders of magnitude.

We can conclude that for this dataset and target distribution, a process-based and stochastic representation give almost identical thermal response for flow rates of 4800 m^3/d and higher, while differences become more exaggerated at low flow rates. This illustrates how a well-designed stochastic model is capable of generating comparable heterogeneous fields to models that include a process-based component.

Adding more complexity to our process-based models with the same dataset does not influence results drastically, which indicates that it can be sufficient to use only reservoir and non-reservoir units. We see some evidence of small-scale variability reducing spread in predicted outcomes and retaining higher production temperatures and delaying breakthrough. Using detailed descriptions of porosity distribution and correlation in each facies could accentuate this effect.

Our investigation was limited to a high N/G ratio with an average of 85%. In this range connectivity is very high and no isolated sand units are present. The expectation is that above our investigated N/G range results will be similar and at lower N/G ranges we expect more difference between methods. Establishing the N/G threshold below which a significant, statistically converged divergence between the stochastic and probabilistic heterogeneity representation occurs will be further investigated.

CRediT authorship contribution statement

Márton Major: Conceptualization, Methodology, Software, Formal analysis, Investigation, Data curation, Writing – original draft, Writing – review & editing, Visualization. **Alexandros Daniilidis:** Conceptualization, Methodology, Software, Formal analysis, Investigation, Data curation, Writing – original draft, Writing – review & editing, Visualization, Project administration. **Thomas Mejer Hansen:** Software, Writing – review & editing. **Mark Khait:** Software, Data curation,

Writing – original draft, Writing – review & editing. **Denis Voskov:** Conceptualization, Methodology, Writing – review & editing, Supervision.

Declaration of Competing Interest

The authors declare that they have no known competing financial interests or personal relationships that could have appeared to influence the work reported in this paper.

Data availability

Data will be made available on request.

Appendix

Optimization of DARTS
Detailed description of optimizing initialization and simulation time in DARTS. The former included:

- Reduction of model input files down to only the rock porosity distribution. The rest of the rock properties were computed from rock porosity on the fly for each model.
- Rock porosity distribution was stored in binary .npy file format using 32-bit floating point data to guarantee fast loading time and minimize disk storage requirements
- Initial conditions were assigned using a temperature and depth gradient. Since the model uses a cartesian mesh, initial conditions could be computed for a single mesh column along the depth axis and consequently copied to all model mesh columns.
- Operator-based linearization (OBL) data was computed only once during the run of the first model in the batch. It was then stored as a binary .pkl file and reused for all subsequent model runs

The optimizations of simulation time included:

- Relaxing of nonlinear and linear tolerances such that the absence of timestep cuts and accuracy of results are guaranteed, but less linear and nonlinear iterations are required.
- Rather aggressive time stepping settings (with first time step of one day, maximum time step of 365 days and time step multiplier of 4) were applied with controlled time-truncation error.
- OBL discretization was set to 16 points, which is sufficient for low enthalpy formulation (Khait and Voskov, 2018)
- AMGX of opensource version 2.2.0.132 was used on the first step of CPR preconditioner (Naumov et al., 2015). Compared to AMGX 2.1, the setup stage performance was significantly improved.
- Single precision of floating-point operations was used for ILU0 preconditioner - the second step of CPR preconditioner. Despite it caused a slight increase in the total amount of linear iterations, each

iteration became significantly cheaper, noticeably improving the overall linear solution time.

The GPU version of DARTS was compiled with CUDA 11.3 toolkit, deployed via docker container on a cloud computing service iRender [https://irendering.net/, in case we need to provide a link to it]. The target computational node was powered by 2 x Intel(R) Xeon(R) CPU E5–2678 v3 and 6 x NVIDIA GeForce RTX 3090 GPU.

References

Babaei, M., Nick, H.M., 2019. Performance of low-enthalpy geothermal systems: interplay of spatially correlated heterogeneity and well-doublet spacings. Appl. Energy 253, 113569. https://doi.org/10.1016/j.apenergy.2019.113569.

Beucher, H., Renard, D., 2016. Truncated Gaussian and derived methods. C.R. Geosci. 348, 510–519. https://doi.org/10.1016/J.CRTE.2015.10.004.

Bredesen, K., Rasmussen, R., Mathiesen, A., Nielsen, L.H., 2021. Seismic amplitude analysis and rock physics modeling of a geothermal sandstone reservoir in the southern part of the Danish Basin. Geothermics 89, 101974. https://doi.org/10.1016/J.GEOTHERMICS.2020.101974.

Bridge, J.S., Leeder, M.R., 1979. A simulation model of alluvial stratigraphy. Sedimentology 26, 617–644. https://doi.org/10.1111/J.1365-3091.1979.TB00935.X.

Bubnova, A., 2018. On the Conditioning of Process-Based Channelized Meandering Reservoir Models on Well Data - Archive ouverte HAL. University of Paris.

Cojan, I., Fouché, O., Lopéz, S., Rivoirard, J., 2005. Process-based reservoir modelling in the example of meandering channel 611–619. 10.1007/978-1-4020-3610-1_62.

Crooijmans, R.A., Willems, C.J.L., Nick, H.M., Bruhn, D.F., 2016. The influence of facies heterogeneity on the doublet performance in low-enthalpy geothermal sedimentary reservoirs. Geothermics 64, 209–219. https://doi.org/10.1016/j.geothermics.2016.06.004.

Crosato, A., 2008. Analysis and modelling of river meandering analyse. Doctoral Thesis, Delft University of Technology, Faculty of Civil Engineering and Geosciences, Delft, The Netherlands.

Daniilidis, A., Doddema, L., Herber, R., 2016. Risk assessment of the Groningen geothermal potential: from seismic to reservoir uncertainty using a discrete parameter analysis. Geothermics 64, 271–288. https://doi.org/10.1016/j.geothermics.2016.06.014.

Daniilidis, A., Khait, M., Saeid, S., Bruhn, D.F., Voskov, D., 2020. A high performance framework for the optimization of geothermal systems, comparing energy production and economic output, in: Proceedings of the World Geothermal Congress. Reykjavik, Iceland, pp. 1–10.

Daniilidis, A., Nick, H.M., Bruhn, D.F., 2021. Interference between geothermal doublets across a fault under subsurface uncertainty; implications for field development and regulation. Geothermics 91, 102041. https://doi.org/10.1016/j.geothermics.2021.102041.

Daniilidis, A., Nick, H.M., Bruhn, D.F., 2020b. Interdependencies between physical, design and operational parameters for direct use geothermal heat in faulted hydrothermal reservoirs. Geothermics 86, 101806. https://doi.org/10.1016/j.geothermics.2020.101806.

DARTS, 2022. Delft Advanced Research Terra Simulator (DARTS) [WWW Document]. URL https://darts.citg.tudelft.nl/.

Feng, R., Balling, N., Grana, D., 2020. Lithofacies classification of a geothermal reservoir in Denmark and its facies-dependent porosity estimation from seismic inversion. Geothermics 87, 101854. https://doi.org/10.1016/J.GEOTHERMICS.2020.101854.

Flumy, 2019. Flumy 5.9 user's guide.

Fuchs, S., Balling, N., 2016. Improving the temperature predictions of subsurface thermal models by using high-quality input data. Part 2: a case study from the Danish-German border region. Geothermics 64, 1–14. https://doi.org/10.1016/J.GEOTHERMICS.2016.04.004.

Fuchs, S., Balling, N., Mathiesen, A., 2020. Deep basin temperature and heat-flow field in Denmark – new insights from borehole analysis and 3D geothermal modelling. Geothermics 83, 101722. https://doi.org/10.1016/J.GEOTHERMICS.2019.101722.

Goovaerts, P., 1997. Geostatistics for natural resources evaluation, geostatistics for natural resources evaluation. Oxford University Press; Applied Geostatistics Series. 10.2307/1270969.

Gringarten, A.C., 1978. Reservoir lifetime and heat recovery factor in geothermal aquifers used for urban heating. Pure Appl. Geophys. 117, 297–308. https://doi.org/10.1007/BF00879755, 1978 117:1.

Haldorsen, H.H., Damsleth, E., 1990. Stochastic modeling. J. Pet. Technol. 42, 404–412. https://doi.org/10.2118/20321-PA.

Hamm, V., Lopez, S., 2012. Impact of fluvial sedimentary heterogeneities on heat transfer at a geothermal doublet scale, in: Proceedings of the World Geothermal Congress. Stanford, California.

Hansen, T.M., 2022. mGstat: a Matlab toolbox of geostatistical tools. 10.5281/zenodo.7074158.

Hill, M.C., Tiedeman, C.R., 2007. Effective groundwater model calibration. Effect. Groundw. Model Calibration. https://doi.org/10.1002/0470041080.

Ikeda, S., Parker, G., Sawai, K., 1981. Bend theory of river meanders. Part 1. Linear development. J. Fluid Mech. 112 https://doi.org/10.1017/S0022112081000451.

Johannesson, H., Parker, G., 1989. Velocity redistribution in meandering Rivers. J. Hydraul. Eng. 115 https://doi.org/10.1061/(asce)0733-9429(1989)115:8(1019).

Keogh, K.J., Martinius, A.W., Osland, R., 2007. The development of fluvial stochastic modelling in the Norwegian oil industry: a historical review, subsurface implementation and future directions. Sediment. Geol. 202, 249–268. https://doi.org/10.1016/J.SEDGEO.2007.05.009.

Khait, M., Voskov, D., 2018. Operator-based linearization for efficient modeling of geothermal processes. Geothermics 74, 7–18. https://doi.org/10.1016/j.geothermics.2018.01.012.

Khait, M., Voskov, D., Zaydullin, R., 2020. High performance framework for modelling of complex subsurface flow and transport applications. In: Proceedings of the ECMOR XVII, 17th European Conference on Teh Mathematics of Oil Recovery. Edinbrugh, UK. EAGE Publications b.v., pp. 1–17.

Larue, D.K., Hovadik, J., 2006. Connectivity of channelized reservoirs: a modelling approach. Pet. Geosci. 12, 291–308. https://doi.org/10.1144/1354-079306-699.

le Ravalec, M., Noetinger, B., Hu, L.Y., 2000. The FFT moving average (FFT-MA) generator: an efficient numerical method for generating and conditioning Gaussian simulations. Math. Geol. 32 https://doi.org/10.1023/A:1007542406333.

Liu, G., Pu, H., Zhao, Z., Liu, Y., 2019. Coupled thermo-hydro-mechanical modeling on well pairs in heterogeneous porous geothermal reservoirs. Energy 171, 631–653. https://doi.org/10.1016/J.ENERGY.2019.01.022.

Lopez, S., Cojan, I., Rivoirard, J., Galli, A., 2009. Process-based stochastic modelling: meandering channelized reservoirs. Analog. Numer. Model. Sediment. Syst. From Underst. Predict. 139–144. https://doi.org/10.1002/9781444303131.CH5.

Lund, J.W., Toth, A.N., 2020. Direct Utilization of Geothermal Energy 2020 Worldwide Review. World Geothermal Congress, pp. 1–39 in.

Matheron, G., Beucher, H., de Fouquet, C., Galli, A., Guerillot, D., Ravenne, C., 1987. Conditional simulation of the geometry of fluvio-deltaic reservoirs. In: Proceedings of the 62nd Annual Technical Conference and Exhibition of the Society of Petroleum Engineers. Dallas, Texas, pp. 27–30.

Mathiesen, A., Nielsen, L.H., Vosgerau, H., Poulsen, S.E., Bjørn, H., Røgen, B., Ditlefsen, C., Vangkilde-Pedersen, T., 2020. Geothermal energy use, country update report for Denmark, in: Proceedings of the World Geothermal Congress. Reykjavik, Iceland.

Mottaghy, D., Pechnig, R., Vogt, C., 2011. The geothermal project Den Haag: 3D numerical models for temperature prediction and reservoir simulation. Geothermics 40, 199–210. https://doi.org/10.1016/j.geothermics.2011.07.001.

Poulsen, S.E., Balling, N., Bording, T.S., Mathiesen, A., Nielsen, S.B., 2017. Inverse geothermal modelling applied to Danish sedimentary basins. Geophys. J. Int. 211, 188–206. https://doi.org/10.1093/GJI/GGX296.

Poulsen, S.E., Balling, N., Nielsen, S.B., 2015. A parametric study of the thermal recharge of low enthalpy geothermal reservoirs. Geothermics 53, 464–478. https://doi.org/10.1016/j.geothermics.2014.08.003.

Remy, N., Boucher, A., Wu, J., 2009. Applied geostatistics with SGeMS: a user's guide. Applied geostatistics with SGeMS: a User's guide 9780521514149, 1–264. 10.1017/CBO9781139150019.

Saeid, S., Al-Khoury, R., Nick, H.M., Barends, F., 2014. Experimental-numerical study of heat flow in deep low-enthalpy geothermal conditions. Renew. Energy 62, 716–730. https://doi.org/10.1016/j.renene.2013.08.037.

Saeid, S., Al-Khoury, R., Nick, H.M., Hicks, M.A., 2015. A prototype design model for deep low-enthalpy hydrothermal systems. Renew. Energy 77, 408–422. https://doi.org/10.1016/j.renene.2014.12.018.

Stefansson, V., 2005. World Geothermal Assessment. Proceedings World Geothermal Congress.

Sun, T., Meakin, P., Jøssang, T., 2001. A computer model for meandering rivers with multiple bed load sediment sizes 2. Computer simulations. Water Resour. Res. 37 https://doi.org/10.1029/2000WR900397.

Vogt, C., Mottaghy, D., Rath, V., Wolf, A., Pechnig, R., Clauser, C., 2010. Quantifying uncertainties in geothermal energy exploration quantifying uncertainty in geothermal reservoir modeling, Proceedings of the World Geothermal Congress.

Voskov, D.V., 2017. Operator-based linearization approach for modeling of multiphase multi-component flow in porous media. J. Comput. Phys. 337, 275–288. https://doi.org/10.1016/J.JCP.2017.02.041.

Wang, Y., Voskov, D., Daniilidis, A., Khait, M., Saeid, S., Bruhn, D., 2020a. Uncertainty quantification of a real low-enthalpy geothermal reservoir. 1st geoscience and engineering in energy transition conference. GET 2020 (2020), 1–5. https://doi.org/10.3997/2214-4609.202021080.

Wang, Y., Voskov, D., Daniilidis, A., Khait, M., Saeid, S., Bruhn David, 2023. Uncertainty quantification in a heterogeneous fluvial sandstone reservoir using GPU-based Monte Carlo simulation. Under Review.

Wang, Y., Voskov, D., Khait, M., Bruhn, D., 2020b. An efficient numerical simulator for geothermal simulation: a benchmark study. Appl. Energy 264, 114693. https://doi.org/10.1016/j.apenergy.2020.114693.

Wang, Y., Voskov, D., Khait, M., Saeid, S., Bruhn, D., 2021. Influential factors on the development of a low-enthalpy geothermal reservoir: a sensitivity study of a realistic field. Renew. Energy 179, 641–651. https://doi.org/10.1016/J.RENENE.2021.07.017.

Weibel, R., Olivarius, M., Kristensen, L., Friis, H., Hjuler, M.L., Kjøller, C., Mathiesen, A., Nielsen, L.H., 2017. Predicting permeability of low-enthalpy geothermal reservoirs: a case study from the Upper Triassic – Lower Jurassic Gassum Formation, Norwegian–Danish Basin. Geothermics 65, 135–157. https://doi.org/10.1016/J.GEOTHERMICS.2016.09.003.

Willems, C.J.L., Nick, H.M., Donselaar, M.E., Weltje, G.-Jan., Bruhn, D.F., 2017. On the connectivity anisotropy in fluvial Hot Sedimentary Aquifers and its influence on geothermal doublet performance. Geothermics 65, 222–233. https://doi.org/10.1016/j.geothermics.2016.10.002.

Zaal, C., Daniilidis, A., Vossepoel, F.C., 2021. Economic and fault stability analysis of geothermal field development in direct-use hydrothermal reservoirs. Geotherm. Energy 9 (12). https://doi.org/10.1186/s40517-021-00193-0.